From compressed- to stretched-exponential dynamics in metallic glasses

Birte Riechers [1,*] Achraf Atila [1] Reza Rashidi [1] Fabian Westermeier [2] Michael Sprung [2] and Robert Maaß [1,3,4,†]

[1] *Federal Institute of Materials Research and Testing (BAM), Unter der Eichen 87, 12205 Berlin, Germany*

[2] *Deutsches Elektronen-Synchrotron (DESY), Notkestrasse 85, 22607 Hamburg, Germany*

[3] *Department of Materials Engineering, Technical University of Munich (TUM), 85748 Garching, Germany*

[4] *Department of Materials Science and Engineering, University of Illinois at Urbana-Champaign (UIUC), Urbana 61801, Illinois, USA*

(Received 16 July 2026; revised 2 October 2026; accepted 16 October 2026; published 12 November 2026)

The microscopic dynamics of metallic glasses are fundamentally governed by their out-of-equilibrium state. In this study, we combine synchrotron x-ray photon correlation spectroscopy with atomistic simulations to track the evolution of structural dynamics from the out-of-equilibrium glassy solid into the metaequilibrium state. The experiments reveal a clear transition from compressed- to stretched-exponential dynamics driven by physical aging. In contrast, the simulations consistently exhibit stretched-exponential behavior across all tested conditions, including zero pressure and applied hydrostatic stress. Despite these qualitatively different initial responses, we demonstrate here that both experimental and computational approaches converge toward a common metaequilibrium stretched relaxation shape with $\beta \approx 0.8$. Further, in this regime both experiment and simulation exhibit de Gennes narrowing in the relaxation timescale and shape parameter, a behavior that emerges in the experiments even before the metaequilibrium state is reached. Ultimately, the absence of compressed-exponential dynamics in simulated quenched-in and pressurized states indicates that the experimental as-cast state possesses a distinct dynamical fingerprint whose exact structural origin continues to remain unresolved.

DOI: 10.1103/cx29-r8ht

I. INTRODUCTION

Amorphous materials have advanced many fields of societal importance, such as medicine [1], energy conversion [2], communication technology [3], and data storage [4]. The disordered structure of amorphous matter, lacking long-range order and grain boundaries, is typically exploited in its out-of-equilibrium condition. Naturally, in this state, the system is thermodynamically driven to achieve metaequilibrium, yet kinetically hindered so that structural changes are tied to an ongoing but slow structural recovery. In metaequilibrium, the system is equilibrated through accessible configurational degrees of freedom on the relevant observation timescale, while remaining metastable with respect to the true thermodynamic equilibrium state, the crystal. Various experimental approaches are able to quantify this process of physical aging by measuring macroscopic material properties such as enthalpy [5,6], volume [7], or dielectric permittivity [8–10] as a function of time. For example, tracking enthalpy and the associated loss in impact toughness [11] below the glass transition ($T < T_g$) exemplifies how these properties can change considerably with physical aging. The phenomenological description of such an aging response is based on functions of exponential form [8,12,13], where an empirical but common representative is the Kohlrausch-Williams-Watts (KWW) function [14,15], which is a stretched exponential function with a characteristic timescale τ and shape parameter β:

$$f(t) \propto e^{-(t/\tau)^{\beta}}. \tag{1}$$

For many glass-forming materials and methods, experimental values of the shape parameter are reported as $\beta < 1$ in the metaequilibrium range of the super-cooled liquid at $T > T_g$ [8,16], as well as in the glassy solid domain $T < T_g$ [8,17]. This observation of stretched-exponential dynamics is considered physically sound, given the interpretation of the shape parameter as representative of the width of the relaxation mode spectrum, constructed on the basis of intrinsically heterogeneous dynamics.

An experimental approach that challenges this description is x-ray photon correlation spectroscopy (XPCS) that allows for measurements of a structural decorrelation time of amorphous materials such as polymer, metallic, network, and spin glasses [18–24]. Here, the choice of the probed wave vector, $\mathbf{q}$, allows for the assessment of dynamics across various length scales [25,26] in structurally and dynamically heterogeneous systems. Focusing on metallic glass dynamics, XPCS studies in the supercooled-liquid state yield timescales comparable to those obtained via macroscopic techniques [27,28]. However, tests within the glassy-solid regime reveal a distinctly different outcome: The dynamics are characterized by compressed—rather than stretched—

*Contact author: birte.riechers@bam.de

†Contact author: robert.maass@bam.de

Published by the American Physical Society under the terms of the Creative Commons Attribution 4.0 International license. Further distribution of this work must maintain attribution to the author(s) and the published article's title, journal citation, and DOI.

exponential behavior ($\beta > 1$ vs $\beta < 1$) [20,21,25,29–38]. Both regimes are formally described by the KWW function [Eq. (1)]. The emergence of a shape parameter $\beta > 1$, signifying compressed-exponential dynamics, fundamentally conflicts with established hypotheses regarding the construction of the relaxation mode spectrum. Mathematically, such a distribution of relaxation times is bounded by $\beta \leqslant 1$ and cannot account for compressed-exponential behavior. Consequently, while being phenomenologically captured by the KWW function, the numerous examples of compressed-exponential dynamics observed across diverse glassy systems reflect the limit of such a microscopic interpretation and suggest that these dynamics arise from physical mechanisms that include aspects beyond the shape of relaxation-mode distributions.

Importantly, compressed-exponential dynamics are not unique to XPCS or metallic glasses. They are also prevalent in soft-matter systems such as colloidal gels, concentrated emulsions, and jammed systems, as evidenced by XPCS, dynamic light scattering (DLS), and traditional light scattering techniques [18,39–43]. Furthermore, both the out-of-equilibrium state of the glassy solid and externally applied or internally induced stresses promote compressed-exponential dynamics [19,33,44].

Imposed boundary conditions such as temperature gradients and convection [45] or beam-induced dynamics [22,46] have been proposed as potential explanations for the observed compressed-exponential behavior. Similarly, aging through a strong out-of-equilibrium condition following significant temperature up-jumps has been reported to yield compressed-exponential one-time response functions. This occurs due to pronounced autoacceleration associated with the evolving aging rate of amorphous materials [9,47–52]. These conditions further entail compressed-exponential dynamics in momentary relaxation traces, as demonstrated through the Tool-Narayanaswamy formalism [53,54] for model polymer systems [47], and are representative of the two-time response functions obtained via coherent scattering techniques such as XPCS and DLS.

However, none of these scenarios, namely temperature gradients, beam-induced effects, or autoacceleration, can account for the systematic transition between compressed- and stretched-exponential dynamics observed via XPCS when heating a metallic glass through the glass-transition range [27] and vice versa during cooling [31]. The same systematic transition is observed when external stress is applied to drive a metallic glass toward its yielding transition [38]. In these studies, identical experimental configurations result in either stretched- or compressed-exponential dynamics, systematically depending on temperature and stress as drivers through the glass or yielding transition. Importantly, these transitions occur under conditions that do not involve the temperature-jump-induced autoacceleration described previously. Thus, the "cast-in" state appears to play an important role in the evolution of the dynamics and the emergence of shape parameters $\beta > 1$.

Several theoretical frameworks have proposed a physical rationale for compressed-exponential dynamics through specific mechanistic scenarios. For example, assuming that residual internal stresses dominate the relaxation process, the initiation of stress-driven events is predicted to generate a scaling law with an exponent of $\beta = \frac{3}{2}$ and $\tau_q \sim q^{-1}$. This behavior arises from the superposition of atomic displacements within long-range elastic fields [55]. Alternatively, models invoking ballisticlike dynamics assume that atomic displacements are governed by coherent motion of particle clusters (or nuclei) moving at a velocity v, resulting in an exponent $\beta = 2$ and $\tau_q \sim q^{-1}$ [56]. Molecular dynamics simulations tracking icosahedral clusters of varying extent have explicitly observed compressed-exponential behavior in the glassy state for sufficiently large clusters [57]. Interestingly, when the entire simulation box is considered, the dynamics remain stretched-exponential across all investigated temperatures and wave vectors, suggesting that the compressed response may be localized. Intermittent dynamics have also been proposed to induce super-diffusive behavior through sudden, discrete structural rearrangements [38]. While a comprehensive mathematical framework for this scenario in the glassy-solid domain is still developing, it likely combines elements of stress-driven and ballisticlike dynamics, as predicted by microstructural clustering. Indeed, computational XPCS has linked the intermittent dynamics frequently observed in synchrotron experiments to the emergence and movement of icosahedral clusters [13,58]. Furthermore, the transition between stretched- and compressed-exponential behavior can be described by models assuming the same underlying relaxation events in the glassy-solid and supercooled-liquid regimes. The transition in the dynamical behavior is triggered by the event density: While the density of events is high in the supercooled liquid (stretched-exponential dynamics), cooperative effects between events are attenuated, while a sparse number of events allows for cooperative and thus amplified motion (compressed-exponential dynamics) [59–61]. Despite these advancements, a consensus on the exact origin of compressed-exponential behavior in metallic glasses and soft matter, and its connection to out-of-equilibrium conditions, remains elusive.

Given that systematic transitions between compressed- and stretched-exponential dynamics are driven by temperature and stress, the logical consequence is to assume that this transition should also be observable during isothermal annealing at $T < T_g$. Such an observation would fundamentally strengthen the link between compressed-exponential dynamics and the out-of-equilibrium state. Specifically, if the system is allowed to evolve at a temperature at which it is initially out of equilibrium, it should eventually transition from compressed- to stretched-exponential behavior as the system approaches metaequilibrium. Here, we present the experimentally resolved evolution of the dynamics of a Zr-based metallic glass, measured via XPCS at a temperature well below T_g. Consistent with our hypothesis, we observe a monotonic and complete transition from compressed- to stretched-exponential behavior, directly correlating the compressed-exponential shape ($\beta > 1$) with the out-of-equilibrium condition. These experimental results are supported by atomistic simulations of a ternary model glass aging at a comparable T/T_g-ratio. Although the initial quenched-in states in the experiment and simulation exhibit dissimilar dynamics, the shape parameters

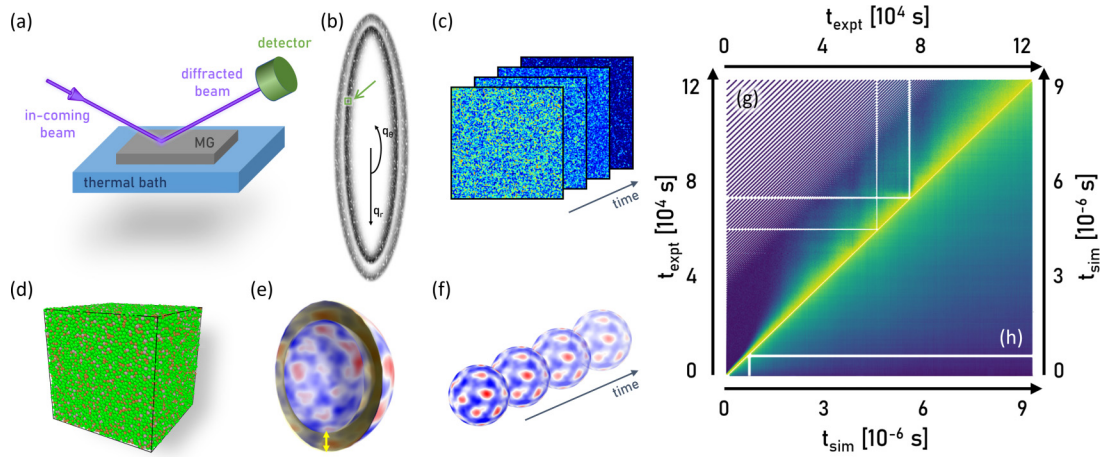


FIG. 1. Schematic illustration of synchrotron [(a)–(c),(g)] and computational [(d)–(f),(h)] XPCS. (a) illustrates the experimental approach in a schematic of the metallic glass (MG) sample on top of the oven surface, measured in reflection. The detector covers only a small range in reciprocal space at the first peak of the structure factor, as indicated by the square in (b) and marked by an arrow. Based on the recorded speckle pattern series illustrated in (c), the two-time correlation function in (g) is calculated (upper-left triangle). (d) illustrates the simulation box of a ternary model glass, indicating icosahedral motifs after 9 μs of simulations. (e) visualizes the diffraction response in reciprocal space, resembling a shell of 0.8 $Å^{-1}$ radial width, located at the first maximum of the structure factor, thereby entailing interference patterns representing the structure at consecutive time steps shown in (f). These speckle patterns are correlated over time, yielding the two-time correlation function from the computational XPCS approach in (h) (lower-right triangle).

characterizing the final metaequilibrium states show excellent agreement within the limits of data accuracy.

II. METHODS AND MATERIALS

A. Synchrotron experiments

A coherent scattering experiment was conducted on a metallic glass sample with the nominal composition $Zr_{52.5}Cu_{17.9}Ni_{14.6}Al_{10.0}Ti_{5.0}$ (Vit105, in atomic %, plate material purchased from Liquidmetal). The sample, with dimensions of 4 × 12 × 1.5 mm^3, was mounted onto the copper surface of a customized oven at beamline P10 of PETRA III (DESY). To prevent oxidation, the oven chamber was continuously evacuated using a turbomolecular vacuum pump. The sample was heated from room temperature (298 K ≈ 0.45 T_g) to the isothermal annealing temperature of 601 K (≈0.9 T_g), where it was held for more than 35 h using a Lakeshore controller [Fig. 1(a)].

The XPCS experiments were performed at an x-ray photon energy of 8.0 keV, corresponding to a wavelength of 1.55 Å. The beam was focused onto the sample to a cross section of 3.3 μm × 2.0 μm, yielding a $1/e$ x-ray penetration depth of 8 μm. The scattered signal was detected in reflection geometry using an Eiger 4M detector (2070 × 2167 pixels, 75 μm pixel size) at a sample-to-detector distance of 2 m, resulting in a per-pixel resolution of $\Delta q = 1.52 \times 10^{-4}$ $Å^{-1}$. The resulting field of view covered a q range of 2.3 to 2.7 $Å^{-1}$ over a similarly narrow azimuthal range along the maximum of the first amorphous diffraction ring [see Fig. 1(b)]. For subsequent analysis, this region was partitioned into q bins of 0.055 $Å^{-1}$ width. During the isothermal annealing experiment, a total of 125 000 two-dimensional speckle patterns [cf. Fig. 1(c)] were recorded with an exposure time of 1 s per frame. To eliminate parasitic scattering and dead pixels, all speckle patterns were filtered using a static, predefined mask isolating active and illuminated pixels across the entire dataset. To account for beam-intensity variations inherent to the top-up operation of Petra III, the intensity of each masked pattern was normalized by the ratio of its frame-averaged intensity to the global average intensity calculated over the entire measurement series.

B. Atomistic simulations

Molecular dynamics (MD) simulations of a ternary $Zr_{65}Cu_{25}Al_{10}$ (in at. %) alloy, serving as a representative proxy for the experimental metallic glass, were performed using an embedded-atom method potential [62] parametrized by Cheng, Ma, and Sheng [63]. Samples containing 64 000 atoms were generated in a cubic box with periodic boundary conditions [see Fig. 1(d)] and equilibrated in the liquid state at 2000 K. The equilibrated liquid was subsequently quenched at a cooling rate of 10^{10} Ks^{-1} to a temperature of $T = 655$ K (≈0.9 T_g), where it was held isothermally for 10 μs. For this cooling rate, the glass transition temperature of the model glass was determined to be $T_g \approx 728$ K. Unless specified otherwise, the simulations were conducted at a constant pressure of 0 MPa; to evaluate the influence of external stress on the relaxation dynamics, additional isothermal simulations were performed at the same temperature under hydrostatic pressures of $P = 40$, 80, 200, and 400 MPa for a duration of 1 μs. Temperature and pressure were regulated using a Nosé-Hoover thermostat and barostat [64]. Structural analysis was executed on atomic configurations saved at regular intervals. Time steps of 0.1 fs and 1 fs were implemented to resolve short-time trajectories for $t < 1$ ps and $t < 1$ ns, respectively, while a time step of 2 fs was utilized for $t > 1$ ns. All MD

simulations were carried out using the LAMMPS package [65], structural analyses were performed via in-house PYTHON scripts, and atomic visualizations were rendered using OVITO [66].

C. Computational x-ray photon correlation spectroscopy

Diffraction patterns were calculated directly from the atomic positions of the MD-generated samples. To minimize artifacts from periodic boundary conditions, scattering vectors were restricted to the reciprocal lattice of the finite cubic simulation cell of side length L,

$$q_\alpha = \frac{2\pi}{L} n_\alpha, \quad n_\alpha \in [-n_q, n_q], \quad \alpha \in \{x, y, z\}, \tag{2}$$

with integer n_α. For the simulated box of approximately $108 \times 108 \times 108$ Å^3, this yields a discrete resolution of $\Delta q \approx 0.058$ Å^{-1}. For each $\mathbf{q}$, the intensity $I(\mathbf{q})$ was evaluated as

$$I(\mathbf{q}) = \frac{1}{N} \left| \sum_j f_j(q) \sum_{k=1}^{N_j} e^{-i\mathbf{q}\cdot\mathbf{r}_k^{(j)}} \right|^2, \tag{3}$$

where N is the total number of atoms, j indexes the atomic species, N_j is the number of atoms of type j, $\mathbf{r}_k^{(j)}$ represents the position of k-th atom of type j, $f_j(q)$ is the atomic form factor for species j, and $q = |\mathbf{q}|$. The atomic form factor $f_j(q)$ was determined using the standard nine-parameter expression for each atom type:

$$f(q) = \sum_{i=1}^{4} a_i \exp\left[-b_i \left(\frac{q}{4\pi}\right)^2\right] + c. \tag{4}$$

The corresponding coefficients were obtained from the *International Tables for Crystallography* [67]. To focus on the principal scattering range of interest, the calculation was restricted in $\mathbf{q}$, sampling the first peak of the static structure factor, $S(\mathbf{q})$, within the interval 2.1 Å$^{-1} \leqslant q \leqslant 2.9$ Å^{-1}. An example of the final 3D $S(\mathbf{q})$ matrix is illustrated in Fig. 1(e). These datasets were saved for subsequent structural and dynamical analysis.

D. Intensity-intensity cross correlation

The speckle patterns obtained from both experiment and simulations were used to compute the intensity-intensity cross-correlation, yielding the two-time correlation function (TTCF) defined as

$$C(\mathbf{q}, t_1, t_2) = \frac{\langle I(\mathbf{q}, t_1) I(\mathbf{q}, t_2)\rangle_q}{\langle I(\mathbf{q}, t_1)\rangle_q \langle I(\mathbf{q}, t_2)\rangle_q}, \tag{5}$$

where $\langle \ldots \rangle_q$ denotes an average over the pixels within a selected q range. For the simulations, this cross-correlation was evaluated using three-dimensional diffraction shells extracted from the atomic trajectories as illustrated in Fig. 1(e). The calculation was performed over consecutive time steps [Fig. 1(f)] for separate q intervals of width 0.1 Å^{-1} spanning from 2.1 to 2.9 Å^{-1}. An analogous approach was applied to the two-dimensional speckle patterns from synchrotron experiments [Fig. 1(c)], which were analyzed separately over consecutive q bins of width 0.055 Å^{-1} ranging from 2.3 to 2.7 Å^{-1}.

The resulting TTCFs are displayed in Figs. 1(g) and 1(h), where the upper and lower diagonals represent the experimental and simulated data, respectively. From these two-dimensional matrices, the one-time intensity correlation functions, $g_2(t_0, t)$, are extracted by taking slices at a fixed waiting time t_0 as a function of delay time $t = t_1 - t_0$. This procedure was for example implemented to capture the initial decorrelation responses at the onset of the isothermal protocol, corresponding to $t_0 = 0$ s for the experiment and $t_0 = 0$ ns for the simulations.

E. Fitting and extraction of timescales

The obtained one-time correlation functions were fitted to KWW functions [cf. Eq. (1)]. To capture the multistep relaxation behavior observed in the atomistic simulations [73], a linear combination of two KWW functions was implemented:

$$g_2(0, t) - 1 = A e^{-2(t/\tau_1)^{\beta_1}} + B e^{-2(t/\tau_2)^{\beta_2}} + C. \tag{6}$$

Here, τ_i and β_i ($i \in \{1, 2\}$) denote the characteristic relaxation time and the shape parameter of the i-th relaxation stage, respectively. The coefficients A and B represent the amplitudes that weight the relative contribution of each decay process, while C is a constant that accounts for the experimental or computational background level. To fit the single-decay decorrelation behavior observed in experiments, a single KWW function was taken into account, corresponding to $i \in 1$ for Eq. (6).

F. Von Mises stress and complementary cumulative distribution function

The local atomic stresses were calculated from the virial theorem [68] as implemented in LAMMPS [65], which yields the six independent components σ_{ab}^i of the symmetric per-atom stress tensor, where $a, b \in \{x, y, z\}$ and i indexes the atoms. From the atomic stress tensor, the von Mises stress σ_{vM} was determined for each atom according to

$$\sigma_{\mathrm{vM}} = \sqrt{\frac{I}{2} + 3J}, \tag{7}$$

where

$$I = (\sigma_{xx} - \sigma_{yy})^2 + (\sigma_{yy} - \sigma_{zz})^2 + (\sigma_{zz} - \sigma_{xx})^2, \tag{8}$$

and

$$J = \sigma_{xy}^2 + \sigma_{xz}^2 + \sigma_{yz}^2. \tag{9}$$

Here, I represents the contribution from differences among the normal stress components, while J represents the contribution from the shear stress components. For each snapshot of the MD trajectory, the per-atom values of σ_{vM} were extracted to construct the complementary cumulative distribution function (CCDF), defined as $\mathrm{CCDF}(\sigma, t) = \mathrm{P}(\sigma_{\mathrm{vM}} > \sigma, t)$. As the bulk of the distribution shifts by only $\sim$0.1 GPa over the total annealing duration, the redistribution of internal local stresses is quantified via the difference with respect to the initial state:

$$\Delta\mathrm{CCDF}(\sigma, t) = \mathrm{P}(\sigma_{\mathrm{vM}} > \sigma, t) - \mathrm{P}(\sigma_{\mathrm{vM}} > \sigma, t = 0), \tag{10}$$

evaluated point-by-point on a common stress grid. The resulting quantity is signed and dimensionless. A negative value, $\Delta\mathrm{CCDF}(\sigma, t) < 0$, implies that fewer atoms exceed the

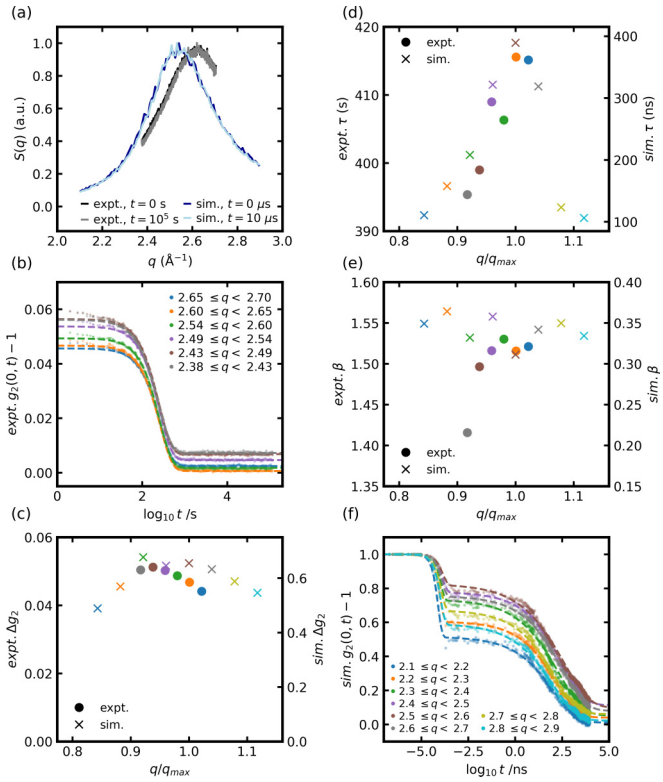


FIG. 2. Structure factor and decorrelation behavior from the as-cast state for a laboratory-cast metallic glass and a simulated model glass. (a) Structure factor, $S(q)$, as a function of wave vector, q, for a laboratory-cast and a simulated glass at the start of the isotherm and after annealing over the time indicated in the legend. (b) One-time correlation functions, $g_2(t_0, t) - 1$ with $t_0 = 0\,\mathrm{s}$, for sequentially binned q windows of $0.055\,\text{Å}^{-1}$ width gained from a laboratory-cast glass together with respective fits to a single KWW function. (c) Decorrelation strength as a function of $q/q_{\max}$ for laboratory-cast and model glasses. (d), (e) Timescale of decorrelation, τ, and shape parameter, β, as functions of $q/q_{\max}$ for laboratory-cast and model glasses based on fits in (b) and (f). (f) One-time correlation functions, $g_2(t_0, t) - 1$ with $t_0 = 0\,\mathrm{ns}$, for sequentially binned q windows of $0.1\,\text{Å}^{-1}$ width gained from the ternary model glass together with respective fits to a double KWW function. In (c)–(e), only the slow relaxation process of the model glass is displayed for comparison with experimental data.

threshold σ at time t than at the start (indicating local stress relaxation), whereas a positive value, $\Delta\mathrm{CCDF}(\sigma, t) > 0$, reveals stress accumulation at that threshold.

III. RESULTS

To quantify the relaxation dynamics from the onset of the isothermal protocol ($t = 0\,\mathrm{s}$), we analyze the XPCS data obtained during annealing at $0.9\ T_g$. Figure 2 displays the experimental static structure factor, $S(q)$, the corresponding one-time correlation function, $g_2(0, t)$, and the resulting fits based on Eq. (6). As shown in Fig. 2(a), $S(q)$ exhibits a broad halo characteristic for amorphous materials, with a maximum located at a wave vector of $q_{\max,\,\mathrm{expt}} = 2.620\,\text{Å}^{-1}$. The overall features of $S(q)$ remain invariant throughout the annealing duration exceeding 10^5 s, with neither oxidation nor crystallization being observed. Further, the peak position exhibits no resolvable shift between the initial and final stages of the isotherm.

The experimental $g_2(0, t)$ [Fig. 2(b)] represents an average over the initial time interval from $t_0 = 0\,\mathrm{s}$ to $t_0 = 400\,\mathrm{s}$ to optimize the signal-to-noise ratio. It exhibits a single relaxation step for all six wave vector ranges. The initial plateau, $g_2(0, 0)$, and the final plateau, $g_2(0, t_{\mathrm{fin}})$, where t_{fin} is the long-time range beyond $10^4\,\mathrm{s}$, display a distinct wave vector dependence. This dependence directly influences the decorrelation strength, $\Delta g_2 = g_2(0, 0) - g_2(0, t_{\mathrm{fin}})$ [Fig. 2(c)], which reveals a systematic, nonmonotonic behavior with a maximum at q values slightly below $q_{\max,\mathrm{expt}}$. Fitting the data with a single KWW function yields the wave vector-dependent decorrelation time, τ, and shape parameter, β, plotted in Figs. 2(d) and 2(e), respectively. Both quantities exhibit a relative increase of 5 % to 10 % across the probed q range.

To evaluate the generality of the experimentally observed structural and dynamical behavior, we complement the synchrotron data with MD simulations of a ternary model glass. This computational framework provides a genuine representation of the generic features of the amorphous state by tracking the aging trajectory toward a well-annealed state over a multimicrosecond timescale, allowing for a qualitative comparison to the experimentally assessed dynamics with a focus on common trends in the wave vector- and time-resolved behavior. Similar multi-microsecond-long protocols have recently yielded significant insights into the microstructural and relaxation features of binary Lennard-Jones model glasses [58,69–73]. The simulated system is characterized by the expected broad amorphous halo in $S(q)$, which remains qualitatively invariant between the initial ($t = 0\,\mu\mathrm{s}$) and final ($t = 10\,\mu\mathrm{s}$) simulation configurations. Figure 2(f) presents the decorrelation behavior of the simulated $g_2(0, t)$ along with the corresponding fits using the double KWW function described by Eq. (6). The high temporal resolution of the simulations captures a fast initial decay at approximately $10^{-5}\,\mathrm{ns}$ to $10^{-4}\,\mathrm{ns}$, reflecting vibrational degrees of freedom. The second decay process, occurring on timescales spanning hundreds of nanoseconds, corresponds to the structural relaxation and is further quantified in Figs. 2(c)–2(e). The simulations access a dynamical window at significantly shorter timescales than the experiments, which is a direct consequence of the spatiotemporal constraints of atomistic modeling. Despite this separation in absolute timescales, the q-dependent trends in the structure and dynamics offer insights into the underlying relaxation mechanisms. In the presented analysis, the extended q range of the simulation data reproduces the observations in the experimental data while providing a broader context. For example, the decorrelation strength plotted in Fig. 2(c) exhibits a similar profile in both approaches, including a distinct maximum slightly below the respective $q_{\max}$. The absolute amplitudes in the simulation are an order of magnitude larger, as expected from the ideal speckle contrast inherent to the computational scattering setup. Furthermore, the timescales $\tau(q)$ exhibit a remarkably similar relative increase up to $q_{\max}$ in both datasets despite a difference by 9 orders of magnitude in absolute numbers [cf. Fig. 2(d)]. Importantly, the extended q range of the simulations captures a subsequent decrease in $\tau(q)$ beyond $q_{\max}$, a regime

not accessed by the experiment. In contrast to the timescale, the shape parameter β reveals pronounced qualitative and quantitative discrepancies between the experiment and the simulation [Fig. 2(e)]. Qualitatively, the experimental data indicate a clear q dependence with a maximum near $q_{\max}$, whereas the computational β values remain strictly q independent across the entire probed range. Quantitatively, the experiment exhibits compressed-exponential dynamics with $\beta \approx 1.55$, whereas the simulations yield strongly stretched-exponential behavior with $\beta \approx 0.35$.

The data presented thus far reflect the dynamical states at the immediate onset of the isothermal protocol, capturing the behavior of the out-of-equilibrium, as-prepared configurations of the sample at elevated temperature. These initial states, i.e., the experimental as-cast and the computational as-quenched structures, are expected to differ significantly due to the vastly different cooling rates and processing histories. Next, we examine the temporal evolution of dynamics as both systems undergo physical aging, allowing us to characterize and contrast their behavior upon approaching the metaequilibrium state.

To this end, Fig. 3 presents the temporal evolution of timescales and shape parameters obtained from KWW fits for both the experimental data in Figs. 3(a), 3(b), and 3(e) and the simulated data in Figs. 3(c), 3(d), and 3(f). Specifically, τ is plotted logarithmically as a function of annealing time in Fig. 3(a) for each of the previously defined q windows. The data show a continuous monotonic increase over time, characteristic of physical aging, before reaching a near-saturation regime at approximately $t > 4 \times 10^4$ s. While differences in aging trajectories across individual q windows are difficult to discern in the main plot, the inset displays the relative variation with respect to $\tau(q_{\max})$. This representation reveals that the timescales collapse onto a single curve at early times ($t < 10^2$ s), but split by up to 15 % for $t > 2 \times 10^4$ s at q values furthest from $q_{\max}$.

Figure 3(b) displays β as a function of annealing time for the individual q windows. Initially, β exhibits values of approximately 1.5 before rapidly decreasing below unity to a level of $\beta \approx 0.8$ on a timeline that closely mirrors the stabilization of τ. Consequently, the dynamics transition from compressed-exponential in the initial out-of-equilibrium state to stretched-exponential in the long-time metaequilibrium state during the annealing protocol. Throughout this process, the temporal evolution of β is q independent. As demonstrated in the inset, the relative variations between the $\beta(q)$ curves remain essentially constant over the entire experimental window.

The atomistic simulations similarly allow tracking of the evolution of τ and β, with the corresponding results summarized in Figs. 3(c) and 3(d). Here, τ exhibits an aging profile qualitatively similar to the experiment, characterized by a monotonic increase that eventually plateaus in the long-time limit ($t > 2000$ ns). However, due to finite-size statistical fluctuations inherent to the computational approach, a relative normalization analysis analogous to the experimental inset could not be resolved. Interestingly, and in striking contrast to the experimental trend, the simulated shape parameter evolves toward a less stretched-exponential behavior, increasing from an initial out-of-equilibrium value of $\beta \approx 0.35$ up to $\beta \approx 0.8-1.0$ at late times. As a result, the short-time out-of-equilibrium dynamics diverge radically between the experiment and the simulation, while the shape parameters ultimately converge to a remarkably similar value of $\beta \approx 0.8$. This convergence indicates that the achieved metaequilibrium states attained at long times share common underlying dynamical features irrespective of the initial processing history.

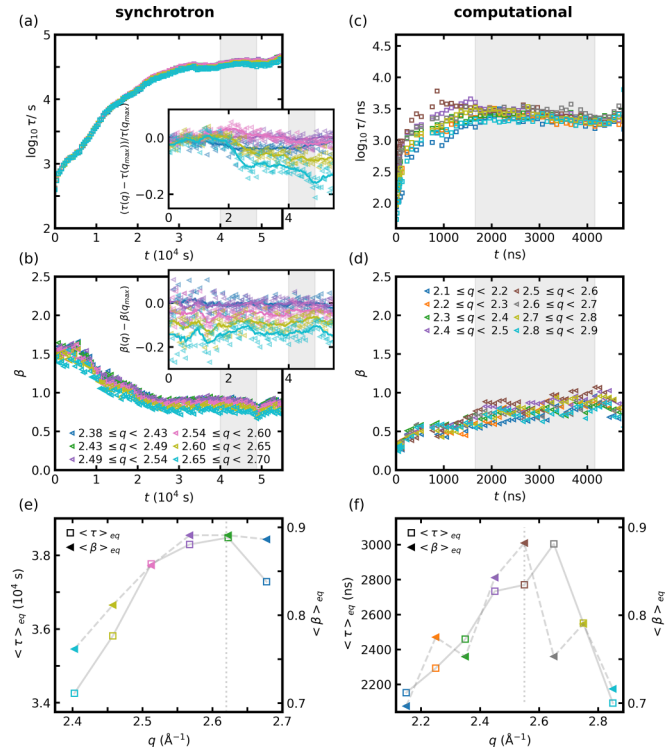


FIG. 3. Evolution of structural dynamics quantified by fits to KWW functions throughout isothermal annealing at 0.9 T_g of a laboratory-cast metallic glass [(a), (b), (e)] and a simulated model glass [(c), (d), (f)]. (a), (b) Logarithmic timescale, $\log_{10}\tau$, and shape parameter, β, of the laboratory-cast glass as a function of annealing time for six wave vector ranges. The insets show the wave vector-specific relative change in timescale, $(\tau(q)-\tau(q_{\max}))/\tau(q_{\max})$, in (a) and the difference in shape parameter, $\beta(q)-\beta(q_{\max})$, in (b) with respect to the values at the position of the maximum of the structure factor, $q_{\max}$. Points in the insets reflect the full data resolution, while solid lines represent smoothed data to highlight underlying trends. The gray shading indicates the time window identified as the metaequilibrium state. The legend in (b) also applies to (a) and the corresponding insets. (c), (d) Logarithmic timescale, $\log_{10}\tau$, and shape parameter, β, of the model glass as a function of linear annealing time for eight wave vector ranges. The legend in (d) also applies to (c). (e), (f) Mean timescale, $\langle\tau\rangle_{\text{eq}}$ (left y axis), and mean shape parameter, $\langle\beta\rangle_{\text{eq}}$ (right y axis), reflecting the equilibrated sample state of the laboratory-cast and the model glass, respectively. Vertical gray dotted lines indicate the position of $q_{\max}$. Lines connecting the data points serve as guides to the eye.

This similarity is further substantiated by the q-resolved behavior in τ and β for both the experimental and the simulated samples at long times. Figures 3(e) and 3(f) present these quantities averaged over the late-stage metaequilibrium regime for experiment and simulations, respectively. When plotted against the wave vector, $\tau(q)$ and $\beta(q)$ exhibit a

distinct maximum located precisely at the position of the principal peak of the static structure factor, $q_{\max}$. Remarkably, this manifestation of de Gennes narrowing occurs irrespective of sample type, appearing clearly in both the experimental datasets and the simulated trajectories, despite the lower statistical resolution of the latter.

IV. DISCUSSION

Compressed-exponential dynamics constitute a systematically observed, but not yet well understood phenomenon across numerous XPCS and DLS studies on amorphous solids [18,39–43]. In this work, we present complementary experimental and simulated XPCS datasets for metallic glasses during isothermal annealing well below the glass transition ($T = 0.9\ T_g$), enabling us to track the structural relaxation and continuous evolution of the shape parameter β from out-of-equilibrium to metaequilibrium conditions.

Scrutinizing the early stages of the isothermal protocol, the laboratory metallic glass initially exhibits compressed-exponential dynamics characterized by a shape parameter of $\beta \approx 1.5$. Despite remaining far from equilibrium in its as-cast state, as evidenced by the ongoing temporal evolution of both the timescale and the shape parameter, the characteristic timescales begin to exhibit a distinct wave vector dependence characteristic of de Gennes narrowing [74,75] as early as $t \approx 2.5 \times 10^4$ s. While this phenomenon is conventionally observed within the stable liquid or the metaequilibrium of the supercooled liquid state, it is reported here in an out-of-equilibrium configuration and notably persists deep within the glassy solid regime. Remarkably, the shape parameter $\beta(q)$ reflects de Gennes narrowing behavior from the earliest annealing stages onward, long before the fitted timescale or shape parameter values stabilize.

When inspecting the early stages of the simulated annealing protocol, in contrast, signatures of strongly stretched-exponential dynamics with $\beta \approx 0.35$ are observed. Hence, the quenched-in configuration of the model glass fails to replicate the compressed-exponential dynamics observed in the laboratory-cast metallic glass. This divergence directly highlights the contrast in quenching conditions and dynamics inherent to experiment and simulation. While the two annealing approaches provide complementary insights, the macroscopic origin of compressed-exponential dynamics cannot be deduced from this data alone. To systematically test the hypothesis that compressed-exponential dynamics originate from either the presence of high internal residual stresses [55] or stress-driven ballisticlike transport, we implement an alternative set of simulations in which the simulation box is subjected to a hydrostatic pressure protocol.

Under the premise that internal residual stresses drive the emergence of compressed-exponential dynamics and quantify the degree of departure from metaequilibrium, Fig. 4 tracks the temporal evolution of the atomic von Mises stresses for simulated configurations subjected to various amplitudes of hydrostatic pressure. Across all explored pressure levels, including zero applied pressure, the mean von Mises stress decreases continuously over time, as illustrated in Fig. 4(a). Concurrently, its standard deviation, plotted in Fig. 4(b),

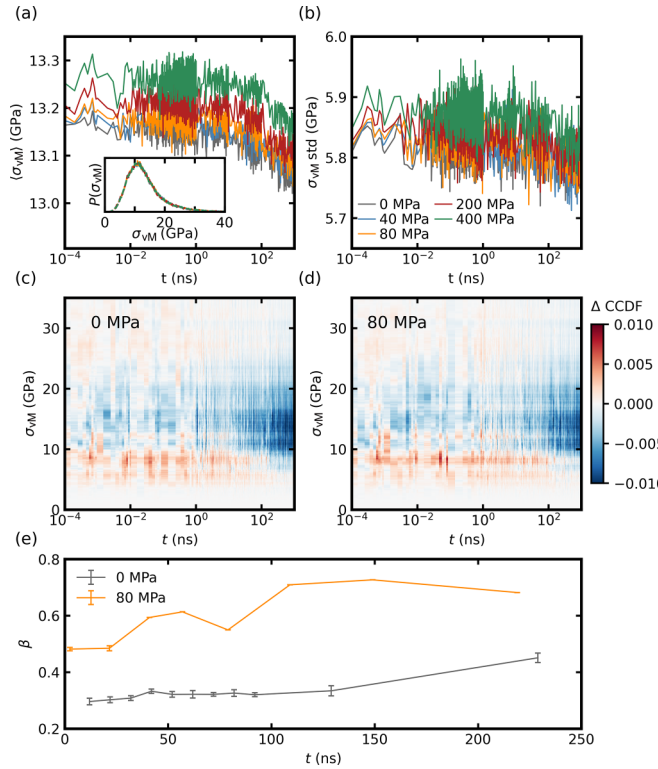


FIG. 4. Temporal evolution of the per-atom von Mises stress distribution of simulated $Zr_{65}Cu_{25}Al_{10}$ at 655 K under five different applied pressure amplitudes (0, 40, 80, 200, and 400 MPa) over 7 orders of magnitude of time from 10^{-4} ns to 10^3 ns. (a) Spatially averaged von Mises stress, $\langle\sigma_{vM}\rangle$, as a function of time for various pressure amplitudes. The inset depicts the atom-specific distribution of von Mises stress for various pressure amplitudes. (b) Standard deviation of the per-atom von Mises stress distribution as a function of time, connected to the averaged quantity plotted in (a). The legend in (b) applies to (a) as well. (c), (d) Color maps of the difference in complementary cumulative distribution functions (CCDFs) of von Mises stress and time, $\Delta\mathrm{CCDF}(\sigma_{vM}, t)$, at 0 and 80 MPa applied pressure, respectively. Red indicates regions where more atoms exceed the given stress level than at time $t = 0$ (stress accumulation), while blue indicates fewer atoms exceeding the given stress level than at time $t = 0$ (stress relaxation). (e) Shape parameter derived from a fit of decorrelation data connected to structural relaxation to a KWW-function at 0 and 80 MPa, averaged over a wave vector range $2.3\,\text{Å}^{-1} \leqslant q \leqslant 2.8\,\text{Å}^{-1}$. In all panels, data at times $t \leqslant 10^{-3}$ ns reflect vibrational motion, while at larger times, structural relaxation becomes the dominating transport mechanism.

exhibits a similar decline, indicating a systematic narrowing of the distribution of local internal stresses around the mean von Mises stress as a function of physical aging. To facilitate a direct comparison of the local stress probabilities over time, the difference in the complementary cumulative distribution functions (CCDFs) of von Mises stress, $\Delta\mathrm{CCDF}(\sigma_{vM}, t) = \mathrm{P}(\sigma_{vM} > \sigma, t) - \mathrm{P}(\sigma_{vM} > \sigma, t{=}0)$, is plotted in Figs. 4(c) and 4(d) for 0 and 80 MPa pressure amplitudes, respectively. On short time scales ($t \leqslant 10^{-3}$ ns), where vibrational degrees of freedom dominate the response, $\Delta\mathrm{CCDF}(\sigma_{vM}, t)$ fluctuates symmetrically around zero. At longer times, as structural relaxation takes over as the dominant transport

mechanism, $\Delta\mathrm{CCDF}(\sigma_{\mathrm{vM}}, t)$ continues to fluctuate near zero until approximately $t \approx 10^0$ ns. Beyond this time, the quantity exhibits a systematic negative shift, indicating a decreasing fraction of atoms exceeding intermediate-to-high stress thresholds, which directly implies local stress relaxation over time. Notably, no discernible features indicating a change in dynamics or underlying mechanism are resolved at 80 MPa or any other tested hydrostatic stresses, as the response remains qualitatively similar to data gained at 0 MPa. Hydrostatic stress does, however, exert a systematic effect on the shape parameter as shown in Fig. 4(e). Specifically, applied stress shifts the shape parameter to higher initial values ($\beta \approx 0.5$ at $t = 0$ s), followed by a rising trend up to $\beta \approx 0.7$ at $t = 200$ ns, which defines the limit of the reliable fitting range for the KWW-function. Hence, hydrostatic stress introduces a distinct upward offset to the shape parameter throughout its temporal evolution, even though the relaxation remains strictly within the stretched-exponential regime ($\beta < 1$) across all tested pressure amplitudes. Given this outcome, the simulations do not provide unambiguous evidence regarding the microscopic origin of compressed-exponential dynamics. Indeed, quenched-in stress fields and long-range elastic stress redistribution might lead to stronger shear-stresses (as captured by von Mises stress) and thus qualitatively different effects than the imposed hydrostatic pressure. However, even under the hydrostatic pressure condition the results demonstrate how internal stresses reduce the stretched decorrelation behavior.

Beyond this, a particularly remarkable finding emerges from the comparison between the synchrotron and computational XPCS datasets, which is the convergence of the shape parameter in the long-time limit. This behavior reflects a shared trajectory toward metaequilibrium, as evidenced by data in Figs. 3(b) and 3(d). Next, we examine the details and broader implications of this continuous transition to metaequilibrium driven by physical aging.

For the experimental data, both the timescale and shape parameter vary monotonically with annealing time toward a steady plateau. This behavior is typical for the transition from an out-of-equilibrium as-cast state to metaequilibrium, with both parameters persistently displaying de Gennes narrowing across the probed q range. The attainment of metaequilibrium in the final stages of the experiment is confirmed by the stabilization of the fitting parameters at times exceeding 4×10^4 s [cf. Figs. 3(a) and 3(b)]. The characteristic timescale of the metaequilibrium state, $\tau_{\mathrm{meq}} = 3.2 \times 10^4$ s, matches the relaxation behavior extrapolated from an Arrhenius process ($\tau_{\mathrm{Arr}} \approx 3.5 \times 10^4$ s [76]), which is understood to drive sub-T_{g} equilibration [77]. Throughout the isothermal protocol, β transitions from ≈1.5, a signature of compressed-exponential dynamics in the as-cast state, to a stable value of ≈0.8 at late stages. This parallel plateauing of both parameters firmly verifies the realization of a well-defined metaequilibrium state within the temporal window of the synchrotron experiment. Further, the value of $\beta \approx 0.8$ matches well with metaequilibrium values reported for Zr-based metallic glasses at or below the glass transition derived experimentally by XPCS and other techniques such as dynamical mechanical analysis, volume or stress relaxation [13,78–80].

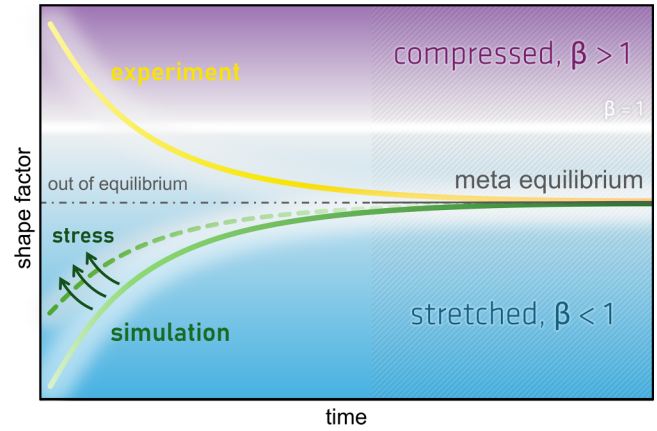


FIG. 5. Schematic representation of the evolution of the shape parameter in experiment and simulation. Background colors indicate the type of exponential behavior with $\beta > 1$ (compressed, purple) in the top part and $\beta < 1$ (stretched, blue) in the bottom part. Note how the metaequilibrium state of both experiment and simulation settles within the regime of $\beta < 1$. The dashed green line and arrows indicate how the shape parameter is shifted to larger values <1 under applied hydrostatic stress as shown in simulations covering the out-of-equilibrium state.

Analogously, the simulations reveal a clear transition from an out-of-equilibrium configuration to a long-time metaequilibrium state. Due to the inherent constraints of atomistic modeling, the observational window is orders of magnitude shorter than in experiments, though it still covers an exceptionally long physical duration of 10 μs. The computational results differ qualitatively from the experimental data in the initial response of β, which exhibits a highly stretched-exponential behavior ($\beta \approx 0.35$) rather than compressed-exponential dynamics. Nevertheless, during the isothermal protocol, both τ and β reach a well-defined plateau in the long-time limit, with τ stabilizing on the order of 10^2 nanoseconds and β systematically increasing from 0.35 to 0.8. During this approach to metaequilibrium state, the mean and standard deviation of the local von Mises stress distribution decrease continuously (cf. Fig. 4 at 0 MPa). This narrowing of the distribution of von Mises stress represents a reduction and homogenization of internal stresses with physical aging, which might be correlated with and thus reflected in the increase of the shape parameter itself.

We conceptualize the key observations regarding the shape parameter in Fig. 5, highlighting that while the experimental dataset yields initial compressed-exponential behavior, the simulation—both in the as-quenched zero-pressure state and under hydrostatic stress—is governed by a different initial mechanism characterized by stretched-exponential dynamics. Despite this initial divergence, both approaches yield a remarkably comparable shape parameter in the long-time limit, reflecting a shared metaequilibrium state dominated by stretched-exponential dynamics with $\beta \approx 0.8$. Furthermore, the application of hydrostatic stress shifts the initial shape parameter upward to $\beta \approx 0.5$ at $t = 0$, which subsequently evolves toward higher values over time. This trend suggests that the stress-altered physical aging pathway might ultimately plateau near the same universal shape parameter

observed in the zero-pressure simulations and experiments. At the same time, this outcome underscores that the simulated systems consistently maintain stretched-exponential behavior across all investigated computational conditions.

V. SUMMARY

We have investigated the evolution of microscopic structural dynamics in a metallic glass across the glassy-solid and supercooled-liquid regimes using synchrotron XPCS experiments and XPCS simulations. Experimentally, the dynamics evolve from compressed- to stretched-exponential relaxation during physical aging, accompanied by systematic changes in both the relaxation time and wave vector dependence. In simulations, physical aging is reflected in structural homogenization and equilibration toward a metaequilibrium state, while the dynamics remain stretched-exponential under all tested conditions, including zero pressure and various levels of hydrostatic stress.

The central outcome of this comparison is that the experiment and simulation converge toward a common metaequilibrium relaxation shape, despite their qualitatively different out-of-equilibrium responses. In both cases, the dynamics level off at a shape parameter of $\beta \approx 0.8$, suggesting a robust relaxation-shape descriptor of the metaequilibrated state. This convergence demonstrates that the long-time aged experimental and computational glasses share a common dynamical signature, even though the experimental as-cast state exhibits compressed-exponential dynamics in contrast to the simulated as-quenched state.

Against this common metaequilibrium limit, compressed-exponential dynamics emerge as a sensitive marker of the initial out-of-equilibrium state of as-cast laboratory metallic glasses. Although such dynamics have been widely associated with stress-driven or elastically mediated rearrangements, the simulations performed here did not develop compressed-exponential behavior under quenching or applied hydrostatic stress. These results therefore indicate that compressed-exponential dynamics encode an experimentally specific feature of the as-cast state, whose structural origin remains a central challenge for connecting laboratory and computational glass dynamics.

ACKNOWLEDGMENTS

The authors thank Peter M. Derlet from PSI for fruitful discussions. The authors acknowledge Deutsches Elektronen-Synchrotron DESY (Hamburg, Germany), a member of the Helmholtz Association HGF, for the provision of experimental facilities. Parts of this research were carried out at PETRA III, beamline P10. Financial support by the European Union's Horizon Europe Framework Programme (HORIZON) under the Marie Skłodowska Curie Grant Agreement (No. 101063523), the Adolf Martens Fond of BAM, the German Research Foundation (DFG, Grant No. 466247278, MA 6338/2-1) and the German Aerospace Center (DLR, Grant No. 50WM2158) are gratefully acknowledged.

B.R., A.A., and R.M. conceived and designed the study. B.R., R.R., F.W., and M.S. conducted x-ray measurements. Beamline data was analyzed by B.R. A.A. performed simulations and their analysis. The manuscript was written by B.R., A.A., and R.M. with the support of all authors. All authors have given approval to the final version of the manuscript.

DATA AVAILABILITY

The data that support the findings of this study are openly available in Zenodo [81].

[1] A. Moeini, T. H. Chinijani, A. M. Khachatourian, M. V. L. Fook, F. Baino, and M. Montazerian, A critical review of bioactive glasses and glass–ceramics in cancer therapy, Int. J. Appl. Glass Sci. **14**, 69 (2023).

[2] J. M. Silveyra, E. Ferrara, D. L. Huber, and T. C. Monson, Soft magnetic materials for a sustainable and electrified world, Science **362**, eaao0195 (2018).

[3] W. C. Wang, B. Zhou, S. H. Xu, Z. M. Yang, and Q. Y. Zhang, Recent advances in soft optical glass fiber and fiber lasers, Prog. Mater. Sci. **101**, 90 (2019).

[4] Microsoft Research Project Silica Team, Laser writing in glass for dense, fast and efficient archival data storage, Nature (London) **650**, 606 (2026).

[5] J. Q. Wang, Y. Shen, J. H. Perepezko, and M. D. Ediger, Increasing the kinetic stability of bulk metallic glasses, Acta Mater. **104**, 25 (2016).

[6] D. Cangialosi, Physical aging and vitrification in polymers and other glasses: Complex behavior and size effects, J. Polym. Sci. **62**, 1952 (2024).

[7] A. J. Kovacs, J. J. Aklonis, J. M. Hutchinson, and A. R. Ramos, Isobaric volume and enthalpy recovery of glasses. II. A transparent multiparameter theory, J. Polym. Sci. Polym. Phys. Ed. **17**, 1097 (1979).

[8] P. Lunkenheimer, R. Wehn, U. Schneider, and A. Loidl, Glassy aging dynamics, Phys. Rev. Lett. **95**, 055702 (2005).

[9] B. Riechers, L. A. Roed, S. Mehri, T. S. Ingebrigtsen, T. Hecksher, J. C. Dyre, and K. Niss, Predicting nonlinear physical aging of glasses from equilibrium relaxation via the material time, Sci. Adv. **8**, eabl9809 (2022).

[10] R. Richert, On the origin of time-aging-time superposition, J. Chem. Phys. **160**, 024501 (2024).

[11] P. Murali and U. Ramamurty, Embrittlement of a bulk metallic glass due to sub-T_g annealing, Acta Mater. **53**, 1467 (2005).

[12] K. Niss, J. C. Dyre, and T. Hecksher, Long-time structural relaxation of glass-forming liquids: Simple or stretched exponential? J. Chem. Phys. **152**, 041103 (2020).

[13] B. Riechers, A. Das, E. Dufresne, P. M. Derlet, and R. Maaß, Intermittent cluster dynamics and temporal fractional diffusion in a bulk metallic glass, Nat. Commun. **15**, 6595 (2024).

[14] R. Kohlrausch, Theorie des elektrischen rückstandes in der Leidener flasche, Ann. Phys. (NY) **167**, 179 (1854).
[15] G. Williams and D. C. Watts, Non-symmetrical dielectric relaxation behaviour arising from a simple empirical decay function, Trans. Faraday Soc. **66**, 80 (1970).
[16] T. Böhmer, F. Pabst, J. P. Gabriel, R. Zeißler, and T. Blochowicz, On the spectral shape of the structural relaxation in supercooled liquids, J. Chem. Phys. **162**, 120902 (2025).
[17] M. Potuzak, R. C. Welch, and J. C. Mauro, Topological origin of stretched exponential relaxation in glass, J. Chem. Phys. **135**, 214502 (2011).
[18] P. Falus, M. A. Borthwick, S. Narayanan, A. R. Sandy, and S. G. J. Mochrie, Crossover from stretched to compressed exponential relaxations in a polymer-based sponge phase, Phys. Rev. Lett. **97**, 066102 (2006).
[19] R. Angelini, L. Zulian, A. Fluerasu, A. Madsen, G. Ruocco, and B. Ruzicka, Dichotomic aging behaviour in a colloidal glass, Soft Matter **9**, 10955 (2013).
[20] M. Leitner, B. Sepiol, L.-M. Stadler, and B. Pfau, Time-resolved study of the crystallization dynamics in a metallic glass, Phys. Rev. B **86**, 064202 (2012).
[21] B. Ruta, Y. Chushkin, G. Monaco, L. Cipelletti, E. Pineda, P. Bruna, V. M. Giordano, and M. Gonzalez-Silveira, Atomic-scale relaxation dynamics and aging in a metallic glass probed by x-ray photon correlation spectroscopy, Phys. Rev. Lett. **109**, 165701 (2012).
[22] J. Baglioni, A. Martinelli, P. Sun, F. Dallari, F. Westermeier, M. Sprung, G. Grübel, and G. Monaco, Uniqueness of glasses prepared via x-ray induced yielding, Rep. Prog. Phys. **87**, 120503 (2024).
[23] V. Scagnoli, S. H. Skjærvø, J. R. Massey, O. Sendetskyi, N. Leo, C. Mazzoli, L. J. Heyderman, and P. M. Derlet, Stretched exponential magnetic relaxation dynamics in artificial square ice revealed through x-ray photon correlation spectroscopy, Phys. Rev. B **112**, 184407 (2025).
[24] R. Maaß and G. Wilde, Metallic glasses: Deciphering their atomic choreography, MRS Bulletin **51**, 1006 (2026).
[25] B. Ruta, G. Baldi, G. Monaco, and Y. Chushkin, Compressed correlation functions and fast aging dynamics in metallic glasses, J. Chem. Phys. **138**, 054508 (2013).
[26] B. Ruta, S. Hechler, N. Neuber, D. Orsi, L. Cristofolini, O. Gross, B. Bochtler, M. Frey, A. Kuball, S. Riegler, M. Stolpe, Z. Evenson, C. Gutt, F. Westermeier, R. Busch, and I. Gallino, Wave-vector dependence of the dynamics in supercooled metallic liquids, Phys. Rev. Lett. **125**, 055701 (2020).
[27] N. Amini, F. Yang, E. Pineda, B. Ruta, M. Sprung, and A. Meyer, Intrinsic relaxation in a supercooled ZrTiNiCuBe glass forming liquid, Phys. Rev. Mater. **5**, 055601 (2021).
[28] P. M. Derlet, B. Riechers, and R. Maaß, Current and future directions in probing structural dynamics and transport of metallic glasses, MRS Bulletin **51**, 1074 (2026).
[29] Z. Evenson, B. Ruta, S. Hechler, M. Stolpe, E. Pineda, I. Gallino, and R. Busch, X-ray photon correlation spectroscopy reveals intermittent aging dynamics in a metallic glass, Phys. Rev. Lett. **115**, 175701 (2015).
[30] X. D. Wang, B. Ruta, L. H. Xiong, D. W. Zhang, Y. Chushkin, H. W. Sheng, H. B. Lou, Q. P. Cao, and J. Z. Jiang, Free-volume dependent atomic dynamics in beta relaxation pronounced La-based metallic glasses, Acta Mater. **99**, 290 (2015).
[31] Z. Evenson, A. Payes-Playa, Y. Chushkin, M. di Michiel, E. Pineda, and B. Ruta, Comparing the atomic and macroscopic aging dynamics in an amorphous and partially crystalline $Zr_{44}Ti_{11}Ni_{10}Cu_{10}Be_{25}$ bulk metallic glass, J. Mater. Res. **32**, 2014 (2017).
[32] I. Gallino, D. Cangialosi, Z. Evenson, L. Schmitt, S. Hechler, M. Stolpe, and B. Ruta, Hierarchical aging pathways and reversible fragile-to-strong transition upon annealing of a metallic glass former, Acta Mater. **144**, 400 (2018).
[33] S. Küchemann, C. Liu, E. M. Dufresne, J. Shin, and R. Maaß, Shear banding leads to accelerated aging dynamics in a metallic glass, Phys. Rev. B **97**, 014204 (2018).
[34] M. Lüttich, V. M. Giordano, S. Le Floch, E. Pineda, F. Zontone, Y. Luo, K. Samwer, and B. Ruta, Anti-aging in ultrastable metallic glasses, Phys. Rev. Lett. **120**, 135504 (2018).
[35] K. Wong, R. P. Krishnan, E. M. Dufresne, K. Ohara, A. R. Sandy, and S. M. Chathoth, Universal aging characteristics of macroscopically and microscopically dissimilar metallic glasses, Acta Mater. **155**, 35 (2018).
[36] A. Das, P. M. Derlet, C. Liu, E. M. Dufresne, and R. Maaß, Stress breaks universal aging behavior in a metallic glass, Nat. Commun. **10**, 5006 (2019).
[37] T. D. Xu, X. D. Wang, Q. P. Cao, D. X. Zhang, and J. Z. Jiang, Aging behaviors in a La-based metallic glass revealed by two-time correlation functions, J. Phys. Chem. C **124**, 22753 (2020).
[38] B. Riechers, A. Das, R. Rashidi, E. Dufresne, and R. Maaß, Metallic glasses: Elastically stiff yet flowing at any stress, Mater. Today **82**, 92 (2025).
[39] L. Cipelletti, S. Manley, R. C. Ball, and D. A. Weitz, Universal aging features in the restructuring of fractal colloidal gels, Phys. Rev. Lett. **84**, 2275 (2000).
[40] L. Cipelletti, L. Ramos, S. Manley, E. Pitard, D. A. Weitz, E. E. Pashkovski, and M. Johansson, Universal non-diffusive slow dynamics in aging soft matter, Faraday Discuss. **123**, 237 (2003).
[41] R. Bandyopadhyay, D. Liang, J. L. Harden, and R. L. Leheny, Slow dynamics, aging, and glassy rheology in soft and living matter, Solid State Commun. **139**, 589 (2006).
[42] K. Lászlo, A. Fluerasu, A. Moussaıd, and E. Geissler, Kinetics of jammed systems: PNIPA gels, in *Macromolecular Symposia* (WILEY VCH Verlag, Weinheim, 2011), Vol. 306, pp. 27–32.
[43] A. Jain, F. Schulz, I. Lokteva, L. Frenzel, G. Grübel, and F. Lehmkühler, Anisotropic and heterogeneous dynamics in an aging colloidal gel, Soft Matter **16**, 2864 (2020).
[44] A. Cornet, G. Garbarino, F. Zontone, Y. Chushkin, J. Jacobs, E. Pineda, T. Deschamps, S. Li, A. Ronca, J. Shen, G. Morard, N. Neuber, M. Frey, R. Busch, I. Gallino, M. Mezouar, G. Vaughan, and B. Ruta, Denser glasses relax faster: Enhanced atomic mobility and anomalous particle displacement under *in-situ* high pressure compression of metallic glasses, Acta Mater. **255**, 119065 (2023).
[45] J. Gabriel, T. Blochowicz, and B. Stühn, Compressed exponential decays in correlation experiments: The influence of temperature gradients and convection, J. Chem. Phys. **142**, 104902 (2015).
[46] A. Martinelli, J. Baglioni, P. Sun, F. Dallari, E. Pineda, Y. Duan, T. Spitzbart-Silberer, F. Westermeier, M. Sprung, and G. Monaco, A new experimental setup for combined fast differential scanning calorimetry and x-ray photon correlation spectroscopy, Synchrotron Radiat. **31**, 557 (2024).

[47] T. D. Jaeger and D. S. Simmons, Temperature dependence of aging dynamics in highly non-equilibrium model polymer glasses, J. Chem. Phys. **156**, 114504 (2022).
[48] V. Di Lisio, V.-M. Stavropoulou, and D. Cangialosi, Physical aging in molecular glasses beyond the α relaxation, J. Chem. Phys. **159**, 064505 (2023).
[49] A. Toda, Isothermal enthalpy relaxation of amorphous polystyrene studied using temperature-modulated fast scanning calorimetry, Thermochim. Acta **721**, 179433 (2023).
[50] R. F. Lancelotti, E. D. Zanotto, and S. Sen, Kinetics of physical aging of a silicate glass following temperature up-and down-jumps, J. Chem. Phys. **160**, 034504 (2024).
[51] M. E. Tracy, B. J. Kasting, C. Herrero, L. Berthier, R. Richert, A. Guiseppi-Elie, and M. D. Ediger, Initial stages of rejuvenation of vapor-deposited glasses during isothermal annealing: Contrast between experiment and simulation, J. Chem. Phys. **161**, 224504 (2024).
[52] A. Y. Amari, L. Costigliola, and J. C. Dyre, Large temperature-up-jump simulations of a binary Lennard-Jones system, Phys. Rev. E **113**, 045411 (2026).
[53] A. Q. Tool, Relation between inelastic deformability and thermal expansion of glass in its annealing range, J. Am. Ceram. Soc. **29**, 240 (1946).
[54] O. S. Narayanaswamy, A model of structural relaxation in glass, J. Am. Ceram. Soc. **54**, 491 (1971).
[55] E. E. Ferrero, K. Martens, and J.-L. Barrat, Relaxation in yield stress systems through elastically interacting activated events, Phys. Rev. Lett. **113**, 248301 (2014).
[56] C. Caronna, Y. Chushkin, A. Madsen, and A. Cupane, Dynamics of nanoparticles in a supercooled liquid, Phys. Rev. Lett. **100**, 055702 (2008).
[57] Z. W. Wu, W. Kob, W.-H. Wang, and L. Xu, Stretched and compressed exponentials in the relaxation dynamics of a metallic glass-forming melt, Nat. Commun. **9**, 5334 (2018).
[58] Z. Wang, B. Riechers, P. M. Derlet, and R. Maaß, Atomic cluster dynamics causes intermittent aging of metallic glasses, Acta Mater. **267**, 119730 (2024).
[59] A. Zaccone, Relaxation and vibrational properties in metal alloys and other disordered systems, J. Phys.: Condens. Matter **32**, 203001 (2020).
[60] K. Trachenko and A. Zaccone, Slow stretched-exponential and fast compressed-exponential relaxation from local event dynamics, J. Phys.: Condens. Matter **33**, 315101 (2021).
[61] V. V. Ginzburg, O. V. Gendelman, and A. Zaccone, Unifying physical framework for stretched-exponential, compressed-exponential, and logarithmic relaxation phenomena in glassy polymers, Macromolecules **57**, 2520 (2024).
[62] M. S. Daw and M. I. Baskes, Embedded-atom method: Derivation and application to impurities, surfaces, and other defects in metals, Phys. Rev. B **29**, 6443 (1984).
[63] Y. Q. Cheng, E. Ma, and H. W. Sheng, Atomic level structure in multicomponent bulk metallic glass, Phys. Rev. Lett. **102**, 245501 (2009).
[64] W. Shinoda, M. Shiga, and M. Mikami, Rapid estimation of elastic constants by molecular dynamics simulation under constant stress, Phys. Rev. B **69**, 134103 (2004).
[65] A. P. Thompson, H. M. Aktulga, R. Berger, D. S. Bolintineanu, W. M. Brown, P. S. Crozier, P. J. in 't Veld, A. Kohlmeyer, S. G. Moore, T. D. Nguyen, R. Shan, M. J. Stevens, J. Tranchida, C. Trott, and S. J. Plimpton, LAMMPS - a flexible simulation tool for particle-based materials modeling at the atomic, meso, and continuum scales, Comput. Phys. Commun. **271**, 108171 (2022).
[66] A. Stukowski, Visualization and analysis of atomistic simulation data with OVITO–the open visualization tool, Modell. Simul. Mater. Sci. Eng. **18**, 015012 (2010).
[67] P. J. Brown, A. G. Fox, E. N. Maslen, M. A. O'Keefe, and B. T. M. Willis, *Intensity of Diffracted Intensities*, International Union of Crystallography (Springer, Dordrecht, 2006), pp. 554–595.
[68] A. P. Thompson, S. J. Plimpton, and W. Mattson, General formulation of pressure and stress tensor for arbitrary many-body interaction potentials under periodic boundary conditions, J. Chem. Phys. **131**, 154107 (2009).
[69] P. M. Derlet and R. Maaß, Emergent structural length scales in a model binary glass - the micro-second molecular dynamics time-scale regime, J. Alloys Compd. **821**, 153209 (2020).
[70] R. Maaß and P. M. Derlet, Micro-plasticity and recent insights from intermittent and small-scale plasticity, Acta Mater. **143**, 338 (2018).
[71] P. M. Derlet and R. Maaß, Micro-plasticity in a fragile model binary glass, Acta Mater. **209**, 116771 (2021).
[72] P. M. Derlet, H. Bocquet, and R. Maaß, Viscosity and transport in a model fragile metallic glass, Phys. Rev. Mater. **5**, 125601 (2021).
[73] A. Atila, Z. Wang, B. Riechers, and R. Maaß, Microstructure-specific mechanisms define multistage relaxation dynamics in a metallic model-glass, arXiv:2606.00323.
[74] P. G. de Gennes, Liquid dynamics and inelastic scattering of neutrons, Physica **25**, 825 (1959).
[75] B. Wu, T. Iwashita, and T. Egami, Atomic dynamics in simple liquid: de Gennes narrowing revisited, Phys. Rev. Lett. **120**, 135502 (2018).
[76] I. Gallino, M. B. Shah, and R. Busch, Enthalpy relaxation and its relation to the thermodynamics and crystallization of the $Zr_{58.5}Cu_{15.6}Ni_{12.8}Al_{10.3}Nb_{2.8}$ bulk metallic glass-forming alloy, Acta Mater. **55**, 1367 (2007).
[77] C. Liu, E. Pineda, D. Crespo, J. Qiao, Z. Evenson, and B. Ruta, Sub-T_g relaxation times of the α process in metallic glasses, J. Non-Cryst. Solids **471**, 322 (2017).
[78] O. Haruyama, K. Yoshikawa, Y. Yamazaki, Y. Yokoyama, and T. Egami, Comparison of structural relaxation behavior in as-cast and pre-annealed Zr-based bulk metallic glasses just below glass transition, Mater. Trans. **56**, 648 (2015).
[79] M. Ikeda and M. Aniya, Correlation between fragility and cooperativity in bulk metallic glass-forming liquids, Intermetallics **18**, 1796 (2010).
[80] P. Luo, P. Wen, H. Y. Bai, B. Ruta, and W. H. Wang, Relaxation decoupling in metallic glasses at low temperatures, Phys. Rev. Lett. **118**, 225901 (2017).
[81] https://doi.org/10.5281/zenodo.23465933.